Biophysical Journal, Volume *114*

Supplemental Information

Probing Mitotic CENP-E Kinesin with the Tethered Cargo Motion Assay and Laser Tweezers

Nikita Gudimchuk, Ekaterina V. Tarasovetc, Vadim Mustyatsa, Alexei L. Drobyshev, Benjamin Vitre, Don W. Cleveland, Fazly I. Ataullakhanov, and Ekaterina L. Grishchuk

Supporting Materials and Methods

Supporting Methods

Experimental procedures

dsDNA sequences. Short dsDNA links were produced using the following primers: (1) biotin-5′-CCT ATC TCG GTC TAT TCT TTT GAT TTA TAA GGG A-3′ and (2) BG-5′-TCC CTT ATA AAT CAA AAG AAT AGA CCG AGA TAG G-3′. Long dsDNA links were prepared using PCR primer (1), as above, and (3) BG-5′-ACC AAG TCA TTC TGA GAA TAG TGT ATG C-3′. The resulting dsDNA sequence for a short link was: biotin-CCT ATC TCG GTC TAT TCT TTT GAT TTA TAA GGG A-BG. Sequence of the long link: biotin-CCT ATC TCG GTC TAT TCT TTT GAT TTA TAA GGG ATT TTG CCG ATT TCG GCC TAT TGG TTA AAA AAT GAG CTG ATT TAA CAA AAA TTT AAC GCG AAT TTT AAC AAA ATA TTA ACG TTT ACA ATT TCA GGT GGC ACT TTT CGG GGA AAT GTG CGC GGA ACC CCT ATT TGT TTA TTT TTC TAA ATA CAT TCA AAT ATG TAT CCG CTC ATG AGA CAA TAA CCC TGA TAA ATG CTT CAA TAA TAT TGA AAA AGG AAG AGT ATG AGT ATT CAA CAT TTC CGT GTC GCC CTT ATT CCC TTT TTT GCG GCA TTT TGC CTT CCT GTT TTT GCT CAC CCA GAA ACG CTG GTG AAA GTA AAA GAT GCT GAA GAT CAG TTG GGT GCA CGA GTG GGT TAC ATC GAA CTG GAT CTC AAC AGC GGT AAG ATC CTT GAG AGT TTT CGC CCC GAA GAA CGT TTT CCA ATG ATG AGC ACT TTT AAA GTT CTG CTA TGT GGC GCG GTA TTA TCC CGT ATT GAC GCC GGG CAA GAG CAA CTC GGT CGC CGC ATA CAC TAT TCT CAG AAT GAC TTG GT-BG.

Additional methods for data analyses

Estimation of the correction factor to compensate for image blurring. In the TCM assay, the CCD camera exposure time for collecting one bead image was 10 ms. During this exposure time, a bead moves continuously due to Brownian motion, and its image becomes slightly blurred, potentially leading to an underestimation of the measured SD. We assessed the extent of this underestimation in our experimental conditions by measuring the SD for Brownian fluctuations of 0.5 μm glass beads held in a laser trap with known stiffness (Fig. S4c). Bead motion was recorded simultaneously with a CCD camera and QPD, which collects bead positions at 100 kHz (10 μs); consequently, the underestimation by QPD is negligible. By extrapolating the ratio of the SDs estimated based on the camera and QPD measurements to zero trapping stiffness, we found that the underestimation in camera recording of an untrapped bead was about 0.7 (Fig. S4d). Because the slope of this dependency is small, potential differences in the blurring effect for tethers with SD of excursions in our experimental range (60-130 nm) were not considered, and the same correction factor was applied to all measurements. Thus, the experimentally determined SDs for bead excursions in the TCM assay were divided by this factor, and these adjusted SD values were compared with model predictions, which are free from blurring.

Plotting the bead clouds. To plot the coordinates of the bead's center in two dimensions (cloud plots), we first calculated the MT-perpendicular bead excursions (Y′-excursions), as described in "Analysis of experimental TCM data" in Materials and Methods. However, the MT-parallel bead excursions (X′-excursions) from the MT-attached motor domains are not known with certainty because the exact position of the motor heads at each time point is unknown. One approach to this problem is to estimate position of the motor from the averaged (smoothed) bead trajectory. This approach seems reasonable because the motor moves much slower than the Brownian motion of the bead (kHz frequency with 50–150 nm amplitude). Thus, for each motor position on the MT, the bead visits many points of the available space. Assuming that the mean bead excursion is close to zero in the moving coordinate system, the position of the motor on the MT in this system can be approximated by the averaged bead positions, such as obtained by smoothing the bead trajectory. By subtracting this estimated position of the motor domain

from the individual X' coordinates of the center of the bead, one can obtain X'-excursions and plot bead clouds. Using this approach, we constructed cloud plots for one representative experiment with a long tether. To examine validity of this approach we used different sliding averaging windows: with 5–250 time points, corresponding to 50–2,500 ms. Three representative plots are shown in Fig. S4e. Clearly, the shape of the cloud in the MT-parallel (X') direction depends on the size of the averaging window. For smoothing sliding windows with larger N, the difference between the smoothed and non-smoothed coordinates is larger, so with increasing N the cloud expands in the MT-parallel direction. Thus, unlike in the traditional TPM assay in which the tether's attachment point is fixed, cloud plots for a motor-transported bead cannot be used for quantitative analysis and we present that only for illustration (Figs. 2d and 4b). Because determining the MT-perpendicular excursions does not involve trajectory smoothing and is free from this artefact, our quantitative conclusions about the tether's properties have been drawn from the MT-perpendicular bead excursions.

Theoretical modeling

Simulation of bead fluctuation dynamics. In the TCM assay, the bead–coverslip link is not stationary, as in the traditional TPM assay (1-5). Instead, the bead moves, carried by a motor (Videos 1, 2). Thus, in the stationary system of coordinates, the bead's trajectory reflects both random bead motion due to thermal noise and its directed transport by the motor (Fig. 1a*).* To take into account the motor's walking, modeling of the TCM was performed using a moving coordinate system (X', Y', Z'), with the origin located on the surface of the MT at the site of motor domain attachment (Fig. 1c). The X'-axis is oriented parallel to the MT pointing toward the plus MT-end. The Y'-axis is perpendicular to the MT and parallel to the coverslip surface, whereas the Z'-axis is perpendicular to the coverslip surface. In our theoretical calculations, this coordinate system moves toward the MT plus-end at 20 μm min^{-1}. Coordinates of the tether-attached bead moving on top of the MT protofilament (α = 0°, Fig. 1c) were calculated in the moving coordinate system (Fig. 1d), and then converted into the real bead coordinates (Fig. 1b). Using these coordinates, bead excursions from the motor's attachment site on the MT were calculated in the MT-parallel (X'-excursions) and MT-perpendicular (Y'-excursions) directions. Histogram distributions of the MT-perpendicular excursions were fitted to Gaussian functions, and their SDs were recorded (Fig. 2 e,f). Note that in real experiments, the velocity of the motor's walking often changed, and the motor also paused stochastically. Therefore, accurate determination of the MT-parallel excursions is not possible, as described in the section "Plotting the bead clouds". Therefore, only the MT-perpendicular bead excursions were used to compare theoretical predictions and experimental results (Fig. 2 e,f).

Estimation of the probability of motor binding to different MT protofilaments. A unique aspect of the TCM assay is that the motor can walk on different MT protofilament tracks. A motor is expected to land with equal probability on different protofilaments of an MT suspended in a solution, but landing on a coverslip-attached MT is sterically limited by the motor's proximity to a coverslip surface, bead diameter and tether's mechanical properties. Although the exact probability function for such a system is not known, its general shape can be deduced based on simple geometrical considerations. Indeed, the probability of the motor landing on the upper MT protofilaments should be maximal (probability 1 for approximately -25° to 25° range of motor-MT attachment angles, Fig. 1c and Fig. S1). In this range, the bead can easily interact with the MT without bending of the tether. The attachment to the coverslip-bound protofilaments, on the other hand, is impossible (probability 0). Binding is also prohibited to protofilaments located closer than 5 nm (the size of the motor's head domain) to the coverslip (probability 0 for attachment angles > 130°). For the remaining protofilaments, the probability of motor binding can be assumed to decrease linearly with increasing binding angle, leading to the "simplified" curve in Fig.

S1b. To test the validity of these assumptions for specific tethers, we randomly generated different motor, tether, and bead configurations. The ratio of the sterically possible configurations to the total number of generated configurations was used as a measure of the binding probability for different protofilaments.

Modeling of motions along different MT protofilaments. To simulate the bead's motion during motor walking along different protofilaments, the first segment of the worm-like chain of the connecting tether was tilted at different angles α along the surface of the 25 nm MT cylinder (Fig. 1c), and bead excursions were calculated as described in section "Simulation of the bead fluctuation dynamics". Histograms of the resultant distributions of the MT-perpendicular bead excursions (Fig. S3a) show that for larger angles of motor attachment, the mean bead position deviates from zero, as observed for α = 0° (Fig. S3b, upper graph). The range of bead motion, as measured from the SD of these distributions (Fig. S3b, bottom graph), decreases with increasing angle, and this effect is stronger for a shorter tether. In real experiments, multiple motor runs are sampled, representing different protofilament tracks, encountered by the motor with different probabilities. To model this situation, we combined bead coordinates obtained for different angles (0°–120°) using weight coefficients corresponding to the probability of the motor landing on different MT protofilaments (Fig. S1b). The weight coefficients for short tethers (5–40 nm) were calculated directly, as described in "Estimation of the probability of motor's binding to different MT protofilaments". For longer tethers, the weight coefficients were estimated using the simplified curve in Fig. S1b, which deviates from the calculated curves by < 12%.

Tether modeling. As described in Materials and Methods section in the main text, bead's tether was modeled as a worm-like chain of 2-nm segments. The model included a rule that prohibited penetration of the tether into the bead, MT or coverslip, but the self-avoidance of the tether was not included. Also, we assumed that the first segment of the chain was anchored perpendicularly to the MT surface. These simplifications are justified by our additional analysis of the anchor point flexibility and the tether self-avoidance**.** We determined SD of Y'-excursions using a modified model in which the chain self-avoidance was implemented by introducing additional rule prohibiting individual links to approach each other closer than 2.5 nm (excluding consecutive links, which are by necessity 2 nm apart). The connection point between MT and the first chain segment was also allowed significant flexibility by selecting rotation angles from Gaussian distribution with SD = 17°. The resulting dependencies for these modified models were very similar to those obtained with our simplified model (Fig. S1c), so taking into account these aspects is not necessary. Also, removing the flexibility of the connection point between the last chain link and the bead had no effect on the SD of Y'-excursions for chains with different PLs.

Modeling of increased dsDNA density. Explicit modeling of numerous dsDNA links is computationally intensive, so we used a highly simplified approach to illustrate a possible effect of increased DNA density. Same modeling framework was used as for a single tether, but we additionally assumed that higher link density increased the effective size of the bead by adding a DNA-representing layer (Fig. S3c). Thermal excursions of the bead tethered to a motor via the 215-nm dsDNA tether were calculated as described in "Simulation of the bead fluctuation dynamics", but the motion of the bead's center was constrained by the sum of bead radius and the layer's thickness, which varied from 0 to 150 nm (Fig. S3d). This DNA-representing layer did not restrict the tether's motion, as the tether was allowed to pass freely through it. This modeling framework may underestimate the effect from high DNA density, so directly modeling multiple tethers would likely reveal even smaller bead excursions.

Length of the compound tethers. To estimate the contour lengths of motor tethers based on the amino acid sequences of K560 kinesin-1 construct (6) and TR CENP-E constructs (7), we calculated the total

lengths of the predicted coiled-coil segments (probability >90%, calculated with "Coils version 2.2" (8)). The 160 amino acids in the coiled-coil segments of K560 correspond to ~24 nm (0.15 nm per residue (9)), whereas the length of the coiled-coil segment in TR CENP-E is ~8 nm. Taking into account the size of the bead-bound antibody molecule (~ 2 nm), the estimated contour length of the TR CENP-E tether is 10 nm. To estimate the length of the short tether, we summed the lengths of its fibrillar parts: 24 nm of K560 kinesin, 12 nm of dsDNA link (0.34 nm per bp (10)), and ~2 nm of SNAP-GBP, yielding a total length of 38 nm. Because the longest part of this tether is formed by the coiled-coil protein segments, we assumed that this tether had PL = 150 nm (11). The long dsDNA tether had same parts as the short tether, but its 557-bp dsDNA link was 189 nm long, so its total contour length was ~215 nm; the PL of this tether was 46 nm, as in the dsDNA (10).

Supporting Table

Table S1. TCM model parameters.

model parameters	**range of values**
tether contour length	4 - 250 nm
tether persistence length	26, 46, 150 nm
length of tether's segment	2 nm
tether "thickness"	0 nm (2.5 nm in Fig. S1c)
flexibility of tether-MT attachment (SD of angular deviation between the last tether segment and bead's normal vector)	not flexible (0^o) (17^o in Fig. S1c)
flexibility of tether-bead attachment (SD of angular deviation between the last tether segment and bead's normal vector)	17^o (0^o in Fig. S1c)
motor angle on MT (corresponding to different protofilaments)	0^o, $\pm30^o$, $\pm60^o$, $\pm90^o$, $\pm120^o$
radius of the bead	250 nm
diameter of MT cylinder	25 nm

Supporting Figures

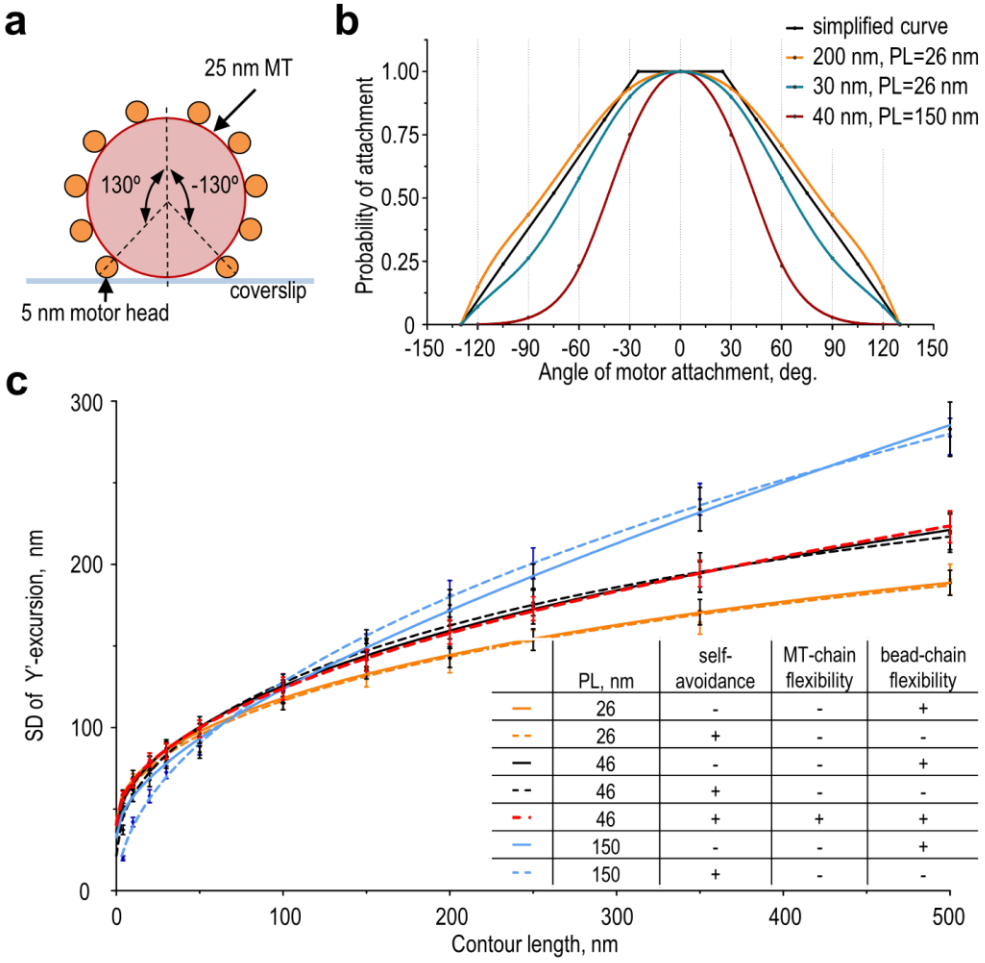

Fig. S1. Geometry of binding of the bead-conjugated motor to the immobilized MT and additional model analyses. (a) Schematic for possible attachment of motor molecules (orange dots) to different protofilaments of the coverslip-immobilized MT cylinder (shown as a cross-section). Protofilaments with attachment angles larger than ±130° are not accessible for motor binding. **(b)** Probability of motor attachment to the MT was calculated for tethers with different contour length and persistence length (PL) as a function of the attachment angle; see Supporting Methods for details. **(c)** Predicted relationship between the SD of Y'-excursions of the bead and contour length for different tethers in TCM assay, see legend to Fig. 1e. Solid lines show same predictions as in Fig. 1e but for a larger range of contour lengths. Broken lines show results for the same model but with a fixed angle of chain attachment to the bead, or for the model in which both ends of the tether were assumed to be flexible and the chain's self-avoidance was implemented (broken red line).

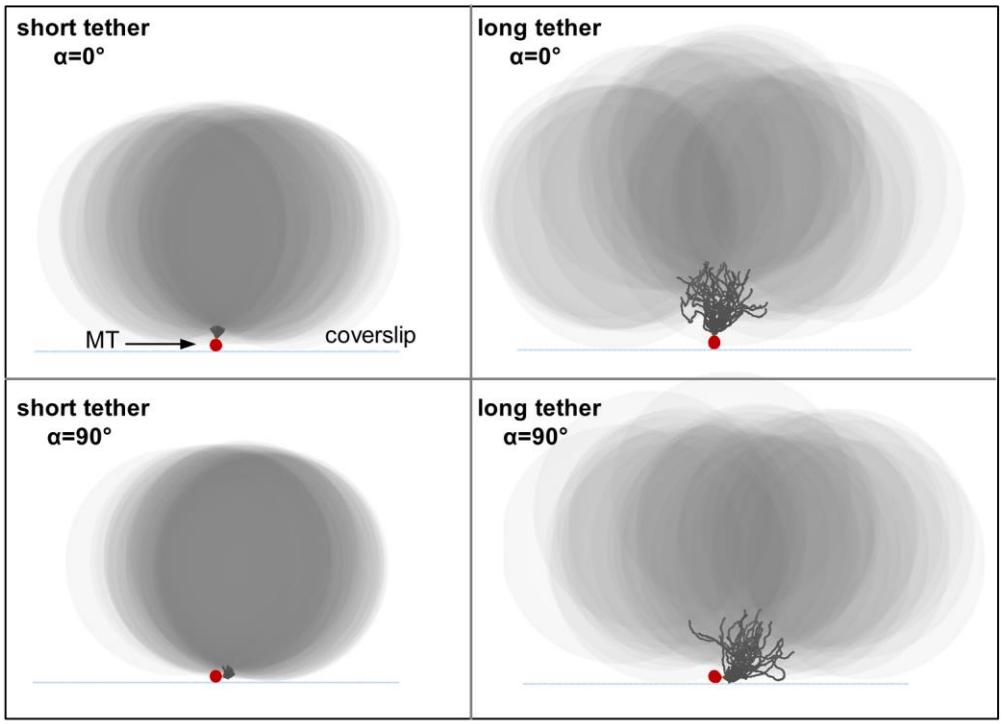

Fig. S2. Impact of the angle of motor-MT attachment on the extent of bead excursions.
Each panel is an overlay of 30 randomly selected frames from Videos 1 and 2, viewed along the MT. Left panels are for the 38-nm tether (as in Video 1), and right panels are for the 215 nm-long tether (as in Video 2); both tethers have PL = 46 nm. Coverslip-immobilized MT is shown in cross-section (red dot), projected bead images as large grey circles, and dsDNA tethers as black lines. The walking motor is in orange, but is almost invisible on this scale. When the motor–MT attachment angle is large ($\alpha = 90^o$, lower panels), the motor walks along the protofilament located close to the coverslips, so bead excursions are more sterically restricted relative to excursions seen with the motor walking on the top MT protofilament ($\alpha = 0^o$, upper panels).

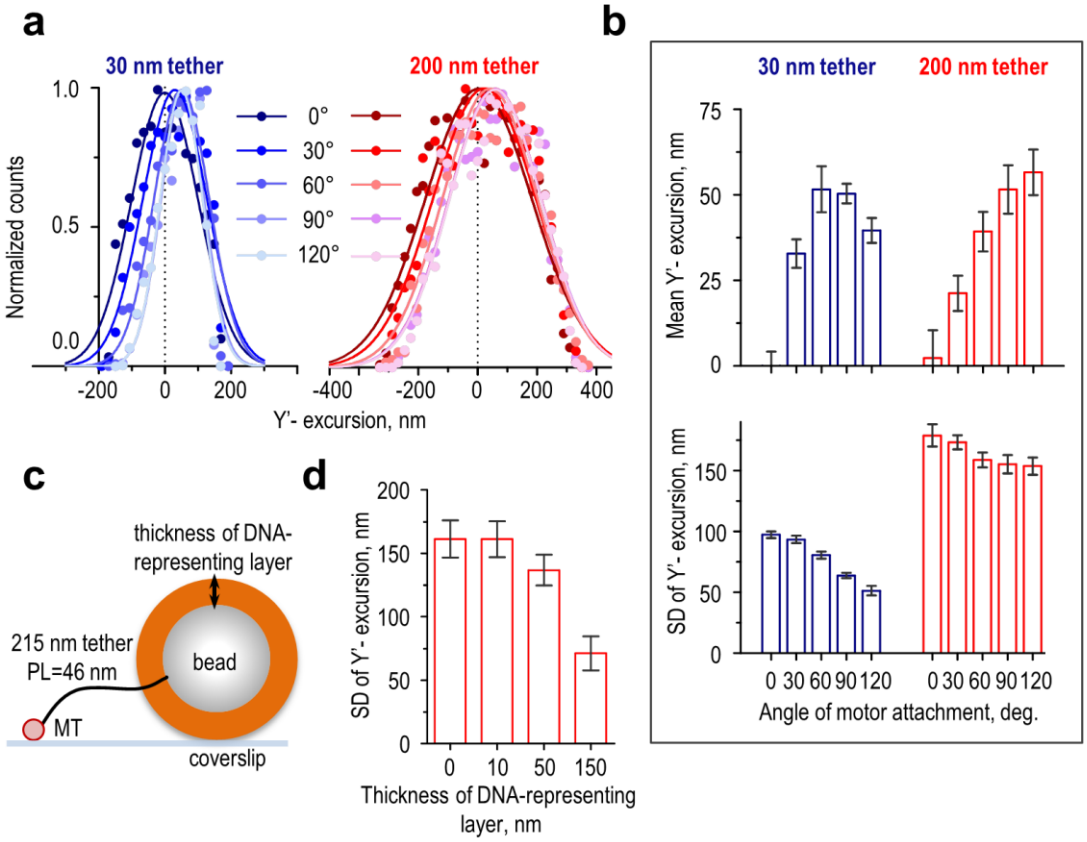

Fig. S3. Additional theoretical analysis of bead excursions. **(a)** Histograms of distributions of MT-perpendicular (Y') bead excursions for indicated angles of motor–MT attachment in the moving coordinate system. Each data set was fit to a Gaussian function and normalized to the mean value. PL = 46 nm; n = 2,000 for each angle. **(b)** Predicted Y'- excursion mean and SD for distributions in panel **a**. Bars are SEMs (top graph) or standard errors (bottom graph) for the Gaussian fits. **(c)** Schematic for modeling bead excursions in the presence of multiple DNA tethers, represented with a layer that constrains bead motions near the coverslip. **(d)** Theoretically predicted SD of MT-perpendicular (Y') bead excursions in the presence of the DNA-representing layers; see Supporting Methods. Error bars are as in Fig. 1e.

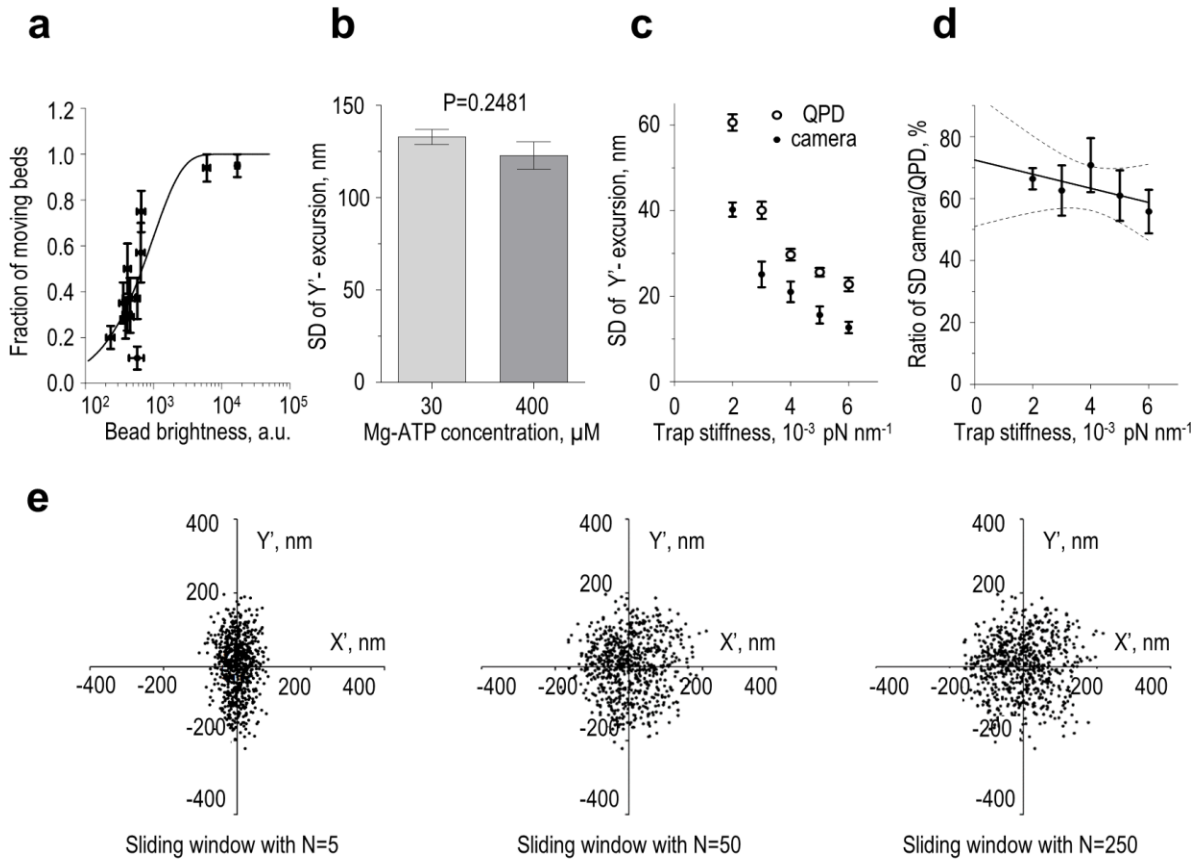

Fig. S4. Additional features of the TCM assay. (a) Fraction of moving beads as a function of coating density, as calculated from kinesin-1–GFP fluorescence intensity. Kinesin-1–GFP was conjugated with long dsDNA tethers. Each data point represents average brightness of ~100 beads from one preparation; percent of moving beads in each preparation was determined by examining ~20 beads. Error bars are SEMs. **(b)** SD of MT-perpendicular (Y') bead excursions in motility experiments with kinesin-1–GFP conjugated via long dsDNA links at two Mg-ATP concentrations. Error bars are SEMs based on 40 beads for 30 μM Mg-ATP or 16 beads for 400 μM Mg-ATP. P-value was determined by two-tailed unpaired t-test. **(c)** SD of bead excursions a function of trap stiffness. Error bars are SEMs. Beads were held in a laser trap, and their coordinates were recorded simultaneously with a CCD camera (10 ms exposure) and QPD (100 kHz). To remove background noise from the QPD amplifier, QPD data are shown after subtraction of the signal obtained in a trap with high stiffness (0.05 pN nm^{-1}). Data are based on 3–5 beads for each stiffness. **(d)** Ratio of SD of bead excursions obtained with a CCD camera to the SD for the same beads recorded by QPD (see panel **c**). Points are mean ± SEM, and the line indicates the results of linear regression (with 95% confidence band). **(e)** Experimental cloud plots for bead excursions obtained for the same bead trajectory, but prepared using different sliding windows that average the MT-parallel component (see Supporting Methods, "Plotting the bead clouds").

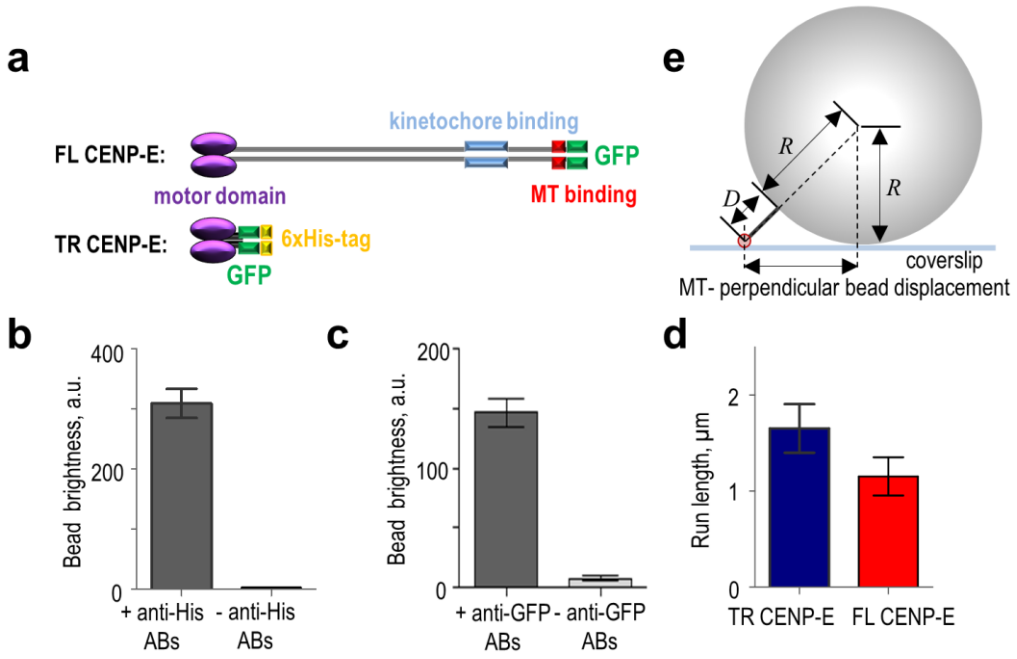

Fig. S5. Supplemental information for experiments with CENP-E. (a) Schematics of the CENP-E proteins used in our assays. **(b)** Brightness of beads coated or not with anti-His antibodies, followed by incubation with TR CENP-E protein tagged with 6His and GFP. Mean ± SEM, n = ~100 beads per sample. **(c)** Brightness of beads coated or not with anti-GFP antibodies, followed by incubation with FL CENP-E protein tagged with GFP. Mean ± SEM, n > 30 beads per sample. **(d)** Run lengths for CENP-E-coated beads. Data are means ± SEM measured for 21 and 18 beads for TR and FL CENP-E, respectively. **(e)** Schematic explaining the relationship between *D* (distance from the surface of the bead with radius *R* to the coverslip-attached MT (cross-section is shown) and the MT-perpendicular displacement of the bead.

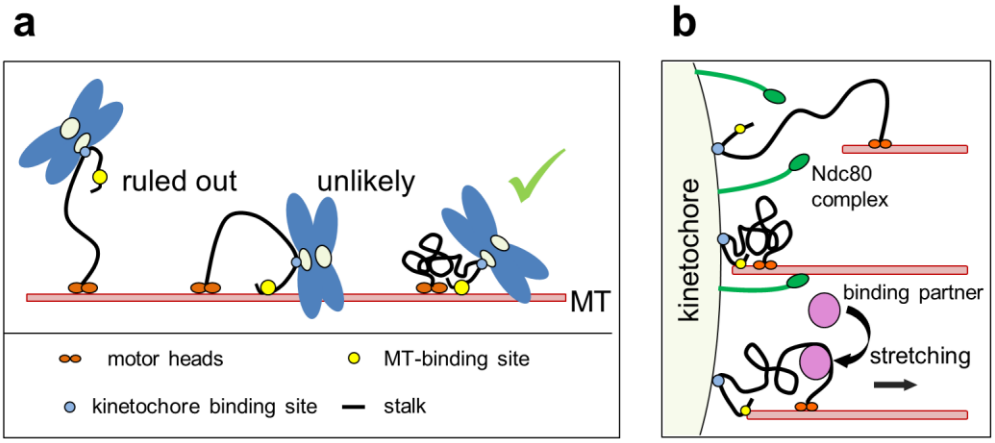

Fig. S6. Implications for kinetochore-MT tethering via CENP-E kinesin. (a) Dynamic CENP-E stalk configurations. Our TCM experiments argue against a model in which the discontinuous coiled-coil stalk of the transporting CENP-E kinesin is extended. The experiments with sideways force suggest that the MT-bound CENP-E is compactly folded. **(b)** Illustration of various CENP-E configurations during mitosis. Early in mitosis, elongated CENP-E may help contact MTs as far as 200 nm away from the kinetochore. However, if CENP-E remains elongated, the kinetochore-associated MT-binding proteins like Ndc80 (shown in green) would not be able to reach the MT (top image). We hypothesize that the compact configuration of CENP-E allows for a shorter distance between the kinetochore and the MT tip, enabling MT-end binding by other kinetochore proteins (center image). Variable tension transduced by the compact CENP-E stalk and causing its partial extension could modulate its binding to various kinetochore partners, thereby mediating a tension-dependent kinetochore response (bottom image).

Video legends

Video 1. Theoretical simulation of a bead attached to a walking motor via a 30-nm tether. The bead-bound motor moves along the coverslip-attached MT (red) in 8-nm steps at 20 μm min^{-1} (one step per frame). The 30-nm tether was modeled as a worm-like chain with PL = 46 nm, similar to the persistence length of dsDNA. Played at 21 fps, the motion appears 2-fold slower than in the model. Bead (0.5 μm in diameter), MT, and tether are drawn to scale.

Video 2. Theoretical simulations of a bead attached to a walking motor via a 200-nm tether. Calculations were performed as for Video 1, but with a 200-nm tether.

Video 3. TCM experiment with a bead moving along a coverslip-immobilized MT. This 0.5-μm bead was coated with 215-nm dsDNA links and kinesin-1 at low density, so its motion is likely to be driven by a single motor. After the bead binds to the MT, it moves along the MT track for ~6 μm until it detaches. Recording was made by DIC with 10-ms exposures, and is played at 100 fps. Scale bar is 2 μm. The MT image was captured separately with 100-ms exposures and overlaid on bead images to achieve better visualization of the MT.

Video 4. Illustration of bead motion relative to the MT in sideways force experiments. The bead (0.5 μm diameter) moves along the coverslip-attached MT (red) in 8-nm steps at 20 μm min^{-1} (one step per frame). Optical trap drives bead oscillations at 1 Hz perpendicular to the MT with an amplitude of 1 μm. Played at 21 fps, the motions appear 6-fold slower than in the model.

Supporting References

1. Brinkers, S., H. R. C. Dietrich, F. H. de Groote, I. T. Young, and B. Rieger. 2009. The persistence length of double stranded DNA determined using dark field tethered particle motion. J Chem Phys 130(21):215105.
2. Han, L., B. Lui, S. Blumberg, J. Beausang, P. Nelson, and R. Phillips. 2009. Calibration of Tethered Particle Motion Experiments. In Mathematics of DNA Structure, Function and Interactions. C. J. Benham, S. Harvey, W. K. Olson, D. W. Sumners, and D. Swigon, editors. Springer New York. 123-138.
3. Nelson, P. C., C. Zurla, D. Brogioli, J. F. Beausang, L. Finzi, and D. Dunlap. 2006. Tethered particle motion as a diagnostic of DNA tether length. J Phys Chem B 110:17260-17267.
4. Pouget, N., C. Dennis, C. Turlan, M. Grigoriev, M. Chandler, and L. Salomé. 2004. Single-particle tracking for DNA tether length monitoring. Nucleic Acids Research 32:e73-e73.
5. Towles, K. B., J. F. Beausang, H. G. Garcia, R. Phillips, and P. C. Nelson. 2009. First-principles calculation of DNA looping in tethered particle experiments. Physical biology 6:025001.
6. Case, R. B., D. W. Pierce, N. HomBooher, C. L. Hart, and R. D. Vale. 1997. The directional preference of kinesin motors is specified by an element outside of the motor catalytic domain. Cell 90:959-966.
7. Kim, Y., J. E. Heuser, C. M. Waterman, and D. W. Cleveland. 2008. CENP-E combines a slow, processive motor and a flexible coiled coil to produce an essential motile kinetochore tether. Journal of Cell Biology 181:411-419.
8. Lupas, A., M. Van Dyke, and J. Stock. 1991. Predicting coiled coils from protein sequences. Science 252:1162-1164.
9. Alberts, B., A. Johnson, J. Lewis, D. Morgan, M. Raff, K. Roberts, P. Walter, J. Wilson and T. Hunt. 2015. Molecular Biology of the Cell, 6th edition: Ch3. “Proteins: The Shape and Structure of Proteins”, p. 116. Garland Science, Taylor and Francis Group, New York , United States.
10. Wang, M. D., H. Yin, R. Landick, J. Gelles, and S. M. Block. 1997. Stretching DNA with optical tweezers. Biophysical journal 72:1335-1346.
11. Wolgemuth, C. W., and S. X. Sun. 2006. Elasticity of alpha-helical coiled coils. Physical review letters 97:248101.